INVITED PAPER *Special Section on Microwave and Millimeter-Wave Technologies*

A Design Method of Transmission-Type Metasurfaces Using Circuit Synthesis Theory of Microwave Bandpass Filters

Hiromichi YOSHIKAWA[†a)], **Nobuki HIRAMATSU**[†], **Masamichi YONEHARA**[†], ***Members***, ***and*** **Hisamatsu NAKANO**[††], ***Fellow***

SUMMARY In this paper, we applied the circuit synthesis theory of filters to the design of transmission-type metasurface cells and arbitrarily designed the amplitude and phase of the transmission and reflection by adjusting the resonant frequency and coupling coefficient. In addition, we successfully designed the phase of the unit cell by using the frequency conversion of filter theory. Moreover, we designed a refractive transmission-type metasurface plate with a novel cell structure that reacts to both polarizations. The prototype operated at the desired refraction angle, confirming the design theory.

key words: *metasurface, transmission-type, refraction, filter theory, bandpass filter*

1. Introduction

In recent years, 5G communication systems have been standardized, and millimeter-wave band communication systems have gained much attraction compared to the microwave band because the millimeter wave band exhibits stronger line-of-sight propagation. This indicates that radio waves are less likely to wrap around obstacles, resulting in coverage holes. This issue can be resolved using transmission-type metasurface plates. A review paper published in 2021 summarized the studies on such metasurfaces and presented the fundamental theory and applications in detail [1]. So far, many applications have been proposed for the transmission-type metasurface. For example, the placement of a metasurface plate directly above an antenna helped to control the directivity of the antenna [2]–[5]. Other notable applications include circular polarizers [6], lenses [7], and refractive plates [1], [8]–[22].

Pfeiffer et al. proposed the use of transmission-type metasurface plates for refraction [8], [9]. In another study, the authors used plates with meander lines and spiral rings to achieve 0 to 2π phase quantity, a key requirement in creating a supercell [10]. Similarly, other studies have also used plates with split-ring resonators [11] and have discussed broadbanding of refractive plates [12]. Another study designed the interface of metasurfaces between the conductor and dielectric considering conductor roughness at 80 GHz [13].

In recent years, metasurfaces have become more complex. For example, the transmission and reflection of metasurfaces can be controlled at different frequencies [14], even nonlinearly [15]. Dual-beam refraction can be obtained by controlling the phase of the metasurface cells [16]. Despite these advances, there is no clear design theory for any of the cell structures in these papers. So, the amplitude and phase of transmission and the amplitude of reflection were determined only as a result of tuning the structural parameters and phase values.

Many papers have designed refractive transmission-type metasurface plates using impedance matrix [17]–[19]. Recently, studies have proposed design methods based on LC equivalent circuits [20], [21]. An *ABCD* matrix has also been proposed as a general design method regardless of cell structures [22]. In these above-mentioned methods, the S-parameters were calculated from an equivalent circuit determined by the structure. Therefore, the final transmission characteristics depend on the results of the optimization.

Unlike the above-mentioned methods, the S-parameters in a bandpass filter (BPF) design method are calculated from a transfer function obtained from the circuit synthesis theory. The S-parameters are then used to calculate an equivalent circuit, and a structure satisfying the equivalent circuit is searched. The coupling matrix, which expresses coupling coefficients between resonators, is calculated from Y parameters [23]–[25]. These design theories have also been applied to antenna design [26]. The transmission and reflection characteristics in these filter design theories are designed based on normalized values of frequency and impedance. In particular, the setting of the input and output impedance values of the circuit from $R = 1\Omega$ to $R = 120\pi\Omega$, which is the impedance of free space, faces no restrictions. Thus, this theory is suitable for the design of transmission-type metasurfaces.

Extracting the coupling matrix from the S-parameters of a filter (either measured or simulated) is an inverse problem, which is generally difficult to solve. Nevertheless, studies have proposed different methods to adjust filter characteristics. One such method involves the calculation of S-parameters from the coupling matrix and optimization of each matrix element to match the measurement results [27], [28]. A few S-parameters are used to determine a transfer function and improve the filter design [29]. These filter tuning tools are also used for designing the unit cell

Manuscript received January 16, 2023.
Manuscript revised March 6, 2023.
Manuscript publicized May 18, 2023.

[†]The authors are with Kyocera Corporation, Yokohama-shi, 220–0012 Japan.
[††]The author is with Hosei University, Koganei-shi, 184–8584 Japan.
a) E-mail: hiromichi.yoshikawa.fj@kyocera.jp

DOI: 10.1587/transele.2023MMI0001

structure of transmission-type metasurfaces.

Notably, the amplitude and phase of transmission and the amplitude of reflection for each cell are guaranteed if the filter theory is applied to each cell of the metasurface, solving one of the design issues for metasurfaces. Also, various proposed filter tuning theories are available for tuning the parameters of these cells.

In this paper, we use frequency transform of the filter design theory to design the transmission and reflection characteristics for the metasurface cells and describe the design flow for a unit cell in detail. Based on the design flow, we show that the proposed novel structure, in which the coupling coefficient is adjusted by the ground electrode, improves the reflection characteristics within the filter bandwidth. In addition, we applied the filter theory to show that the proposed unit cell structure has low loss due to the widened passband.

Based on the filter design theory, we adjusted the phase for each cell by changing its center frequency through frequency conversion and designed a refractive metasurface plate. Note that cost is a critical issue for the proliferation of applications in the millimeter wave range. By using our proposed wideband unit cell design, the refractive plate achieves loss that is low enough for practical use, even with a low-cost FR4 substrate. Finally, the validity of the design was verified using a prototype of the refractive plate.

2. Design of Refractive Plates Using Filter Theory

2.1 Design with Normalized Frequency

The reactance function is used to describe the transmission and reflection functions of a two-port lossless nth-order BPF. The internal resistance at the input port and the load resistance at the output port are normalized to 1. The S-parameters are expressed by the following polynomial equations [24].

$$S_{11} = \frac{F(s)}{\varepsilon_R E(s)} \tag{1}$$

$$S_{21} = \frac{P(s)}{\varepsilon E(s)} \tag{2}$$

where $s = j\Omega$, and ε and ε_R denote coefficients. Ω denotes normalized angular frequency. $P(s)$ denotes a polynomial representing the angular frequency of attenuation poles Ω_p in the transmission function in S_{21}. For $n-1$ attenuation poles or fewer, $\varepsilon_R = 1$. $F(s)$ and $E(s)$ also denote nth-order polynomials determined from the filter functions. The nth-order Chebyshev characteristic functions are described in detail in a previous study [24]. Note that the related formulas are omitted here. With respect to the Chebyshev characteristic bandpass filters, the S-parameters are calculated with different filter orders from $n = 2-4$. Figure 1 shows the calculated results of the amplitude and phase of transmission and the amplitude of reflection with respect to the normalized frequency axes. The phase of transmission and

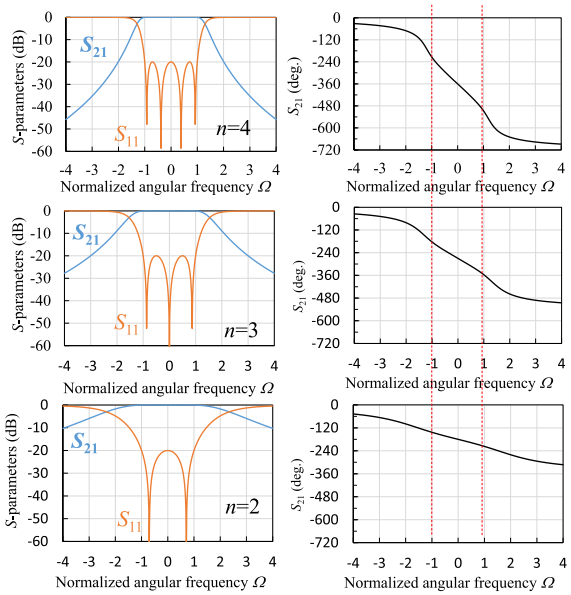

Fig. 1 Calculation results based on filter theory.

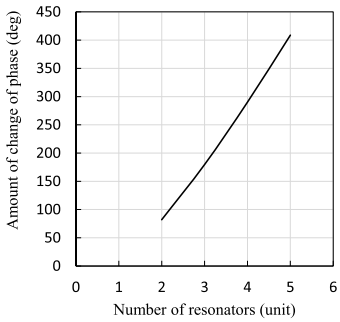

Fig. 2 Relationship between the number of resonators and the phase of the transmission.

the coefficients of transmission and reflection in the metasurface design are in the range of $-1 < \Omega < 1$. According to the calculated results, the transmission phase increases with the number of filter orders in the normalized passband frequency range of $-1 < \Omega < 1$. Figure 2 shows the amount of change in the transmission phase for normalized bandwidths in the range of $-1 < \Omega < 1$. These results show that the transmission phase of the metasurface is determined by the number of resonators and not by its structure.

We use the region in the passband where the phase varies linearly with frequency when designing the supercell. This is because a higher linearity has a small effect on the phase difference by a shift of the frequencies in the same direction.

2.2 Unit Cell Design of Refractive Plates

Here, we designed a refractive plate at 28 GHz. The phase difference between cells, $\Delta\Phi$, in the case of a normal incident wave ($+z$ direction in Fig. 6) is expressed as

$$\Delta\Phi = k_0 d \sin\theta_0 \tag{3}$$

where k_0 denotes the wavenumber in free space, d denotes the distance between cells, and θ_0 denotes the angle of refraction defined in Sect. 2.6.

In a sequence of unit cells with different structures, a supercell is the smallest periodic unit. The phase of each unit cell is shifted by $\Delta\Phi = 2\pi/p$, where p denotes the number of unit cells in the supercell [30]. By using this cell structure, we designed a supercell with a refraction angle of $\theta_0 = 45°$ at 28 GHz. The phase difference for transmission is set to $\Delta\Phi = 90°$. The four unit cells corresponding to the four different phases are referred to as $U(0)$, $U(90)$, $U(180)$, and $U(270)$. As shown in Fig. 2, a supercell with four resonators ($n = 4$) can realize the maximum phase change of 270° required for this refractive plate design. Using Eq. (3), the above values yield a unit cell size of $d = 3.79$ mm.

2.3 Transmission Plate Design with Frequency Conversion

The following frequency conversion is used when designing BPFs to convert normalized frequency to the desired frequency band [24]:

$$\Omega = \frac{f_c}{B_w}\left(\frac{f}{f_c} - \frac{f_c}{f}\right) + j\frac{f_c}{B_w}\frac{1}{Q_u} \tag{4}$$

where f_c denotes the center frequency, B_w denotes the bandwidth, and Q_u denotes the unloaded quality factor of the resonator. Figure 3 show the calculated results of the frequency conversion for the four cells at 28 GHz. The calculation conditions for all cells are $n = 4$, $B_w = 4$ GHz (equi-ripple), $S_{11} < -20$ dB, and lossless. The phase changes arbitrarily at 28 GHz when the center frequency, which is calculated from the lowpass prototype filter by frequency conversion, is shifted. The center frequencies of $U(0)$, $U(90)$, $U(180)$, and $U(270)$ are shifted to $f_c = 26.053$, $f_c = 27.310$, $f_c = 28.666$, and $f_c = 29.823$ (GHz), respectively. Consequently, the phases of $U(0)$, $U(90)$, $U(180)$, and $U(270)$ are −460°, −370°, −280°, and −190°, respectively, with the phase differing by 90° between each cell.

2.4 Coupling Topology of Cell by Coupling Matrix

A coupling matrix $[M]$ having input and output circuits has been proposed in nth-order BPF design [24]. The size of the coupling matrix is $(n + 2) \times (n + 2)$. Its elements M_{ii} $(i = 1, 2, \cdots, n)$ represent the resonant frequency (in GHz in this paper) of the resonators, M_{ij} $(i, j = 1, 2, \cdots, n, i \neq j)$ represent the coupling coefficient of the resonators, and M_{0i} and $M_{i,n+1}$ $(i = 1, 2, \cdots, n+1)$ represent the coupling coefficients (external Q factor Q_e in this paper) between resonator and source/load, respectively. M_{00} and $M_{n+1,n+1}$ represent the coupling coefficients at source and load, respectively, and are usually zero in value. The $(n + 2) \times (n + 2)$ coupling matrix involves a rotation matrix, and its orthogonality is used to transform it into a coupling topology of BPF [24].

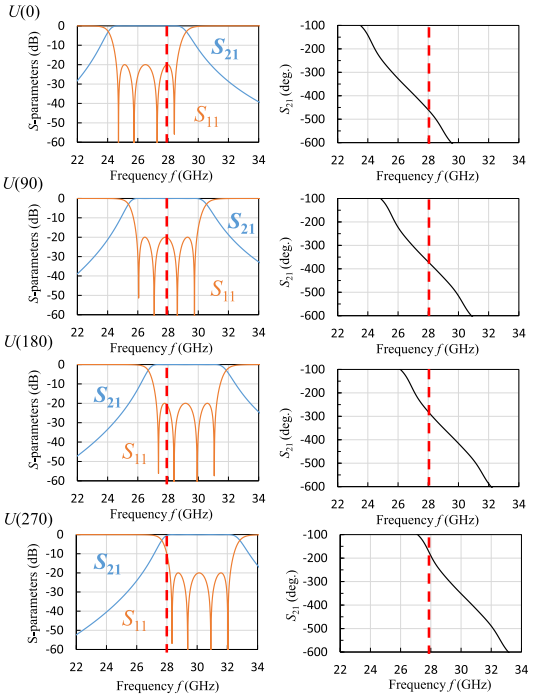

Fig. 3 Calculated results of frequency conversion of BPF with $n = 4$, $B_w = 4$ GHz and lossless.

2.5 Simulation Model of Unit Cell of Refractive Plates

As mentioned in Sect. 2.2, the size of a unit cell is $d = 3.79$ mm. The thickness of each dielectric is 0.48 mm and that of the conductor is 0.018 mm. Thus, the total thickness is 3.006 mm. The rotationally symmetric structure at 90° with respect to the center of unit cell involves no polarization dependence. The unit cell was electromagnetically (*EM*) simulated using the finite element method (FEM; ANSYS HFSS™) with a Floquet Port (plane wave) at both ends under periodic boundary conditions. The unit cell is composed of FR4 substrates (relative permittivity $\varepsilon_r = 4.5$, dielectric loss $\tan\delta = 0.015$, conductivity $\sigma = 2.9 \times 10^7$ S/m) for low cost. Here $\sigma = \sigma_0 \times \sigma_r$, where σ_0 denotes the conductivity of copper (5.8×10^7 S/m), and σ_r denotes relative conductivity.

Reflection characteristics may not be achieved with metasurfaces if the coupling between the resonators is not correctly adjusted [5]. Figure 4 shows the initial structure of the unit cell without adjusting the coupling structure. Here, the initial structure does not include cross-shaped ground electrodes for adjusting the coupling coefficient.

We added electrodes instead of adjusting the thickness so as to adjust the coupling coefficient without increasing the layer thickness. Figure 5 presents the structure of the unit cell proposed in this paper. The resonant frequency of each cell is adjusted by changing the size of resonators in layers 1, 3, 5, and 7, while the coupling coefficients are adjusted by tuning layers 2, 4, and 6.

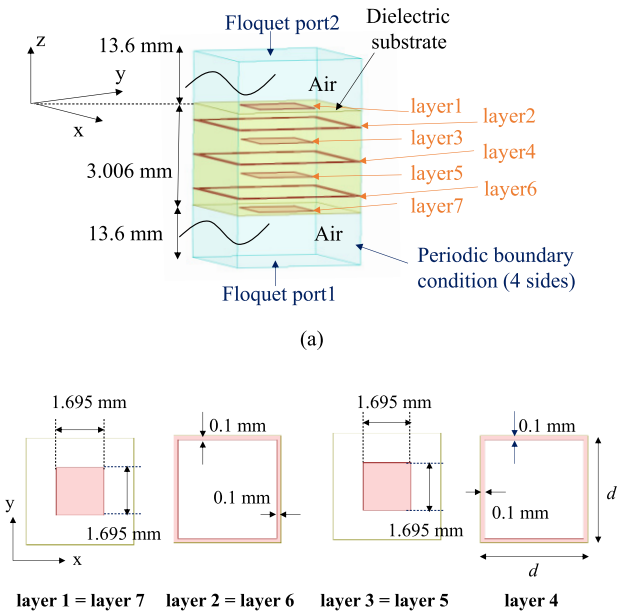

Fig. 4 Initial structure of the unit cell without adjusting the coupling structure. (a) Diagrammatic view. (b) Plane view.

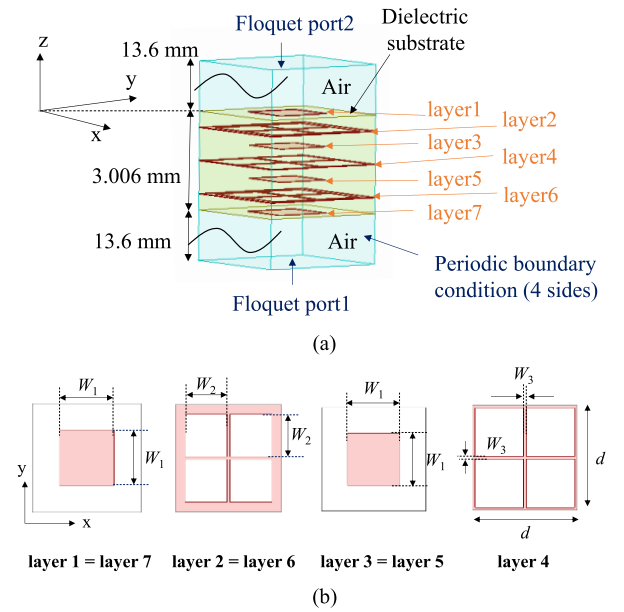

Fig. 5 Proposed structure of the unit cell with adjustment to the coupling structure. (a) Diagrammatic view. (b) Plane view. (W_3 = 0.1 mm in layers 2, 4, and 6)

2.6 Simulation Model of Refractive Plates

Figure 6 shows the simulation model of the refractive metasurface plate. The supercells having 3.79 mm × 300 mm × 3.006 mm consist of four cells. Here, a periodic boundary condition in the range z < 0 and a radiation boundary condition in the range z > 0 are used. A Floquet Port (incident plane wave) is used for excitation. The number of cells is set to 79 cells.

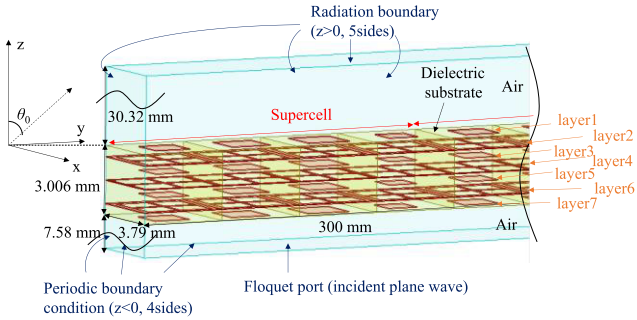

Fig. 6 Simulation model of the refractive metasurface plate.

2.7 Design Flow of Unit Cell

The center frequency f_c of the filter, the bandwidth B_w, and the frequency of the attenuation poles f_p in a typical filter design are determined to meet the required specifications for in-band and out-band and determine the target coupling matrix. Here, the resonance frequency f of the resonator, the external Q factor Q_e, the coupling coefficients k, and the non-adjacent coupling coefficients k' are assumed to be adjustable.

A transmission-type unit cell requires only the phase characteristics in the passband. Generally, the metasurfaces do not have an adjustment mechanism for the coupling between the free space and the first (end) resonator. The non-adjacent couplings in metasurfaces are also nonadjustable. Thus, the structure fixes the extracted values of Q_e and k'.

The values of f_c, B_w, and f_p are used to determine the phase and the values of Q_e and k'. Then, the Chebyshev bandpass filter is used to calculate the target coupling matrix. Only f and k in the matrix are adjusted by the structure. The target matrix is also changed when the structure is changed significantly since the values of Q_e and k' depend on the structure.

Figure 7 shows the design flow of a unit cell. In the figure, the subscripts FT and EM of the variables indicate that the values were determined using the Chebyshev bandpass filter theory (FT) and the S-parameters extracted from EM simulations, respectively. Based on the extraction method in this flow, B_w is defined as the half-power frequency bandwidth. However, Chebyshev's design uses equi-ripple frequency bandwidth. Thus, frequency conversion needs to be performed before comparison with the extraction method so that S_{21} (dB) = −3 dB at $\Omega = \pm 1$. In this flow, the coupling matrix is used as a denormalized coupling matrix in the bandpass frequency domain. Therefore, the frequency (in GHz) and coupling coefficient are obtained after frequency conversion.

a) Number of resonators n is determined from design frequency and phase change.
b) The nth-order Chebyshev bandpass filter characteristics are calculated.

c) *EM* simulator model is created as a periodic structure of a unit cell consisting of n resonators.
d) S-parameters are obtained by *EM* simulation.
e) Transfer function is obtained using the parameter extraction method [29]. The bandwidth B_{wEM} (half-power frequency bandwidth), unloaded Q factor Q_{uEM}, and the attenuation pole frequencies Ω_{pEM} are determined from attenuation poles.
f) Coupling matrix $[M_{EM}]$ is calculated from the transfer function extracted from *EM* simulation.
g) As shown in Fig. 3, the phase at the design frequency is adjusted by frequency conversion. The Q_{eFT} is adjusted by the bandwidth B_{wFT} (half-power frequency bandwidth). Here, the attenuation pole frequencies Ω_{pFT} and the unloaded Q factors Q_{uFT} given in the coupling matrix calculation using the filter theory are the same values as Ω_{pEM} and Q_{uEM} extracted from *EM*-simulated S-parameters.
h) Ideal coupling matrix $[M_{FT}]$ is calculated from the transfer function of the filter theory.
i) f_{cFT} and B_{wFT} are adjusted so that the theoretically calculated external Q values, Q_{eFT}, and $S_{21,FT}$(phase) match the reference values Q_{eEM} and the desired phase. (Loop g)-i))
j) Resonance frequencies f_{FT} and coupling coefficients k_{FT} of $[M_{FT}]$ are compared with the resonance *frequencies* f_{EM} and coupling coefficients k_{EM} of $[M_{EM}]$ of the unit cell. The structural pattern of the unit cell is adjusted to match the above values.
(Loop c)-j) including loop g)-i))

The non-adjacent couplings k'_{FT} are adjusted by the position of the attenuation poles. (loop j)) However, it is difficult to achieve perfect agreement between k'_{FT} and k'_{EM} when the reflection characteristics differ. Here, the difference in the values of k'_{FT} and k'_{EM} in the coupling matrices $[M_{FT}]$ and $[M_{EM}]$ are sufficiently smaller than the values of main couplings between adjacent resonators.

In general, a wideband BPF is used to achieve low loss. Here, Q_e is small. Figure 8 shows the calculation results for two BPFs of different bandwidths with the same $Q_u = 58$ (calculated from the properties of FR4 used in the prototype). The blue line corresponds to $f_c = 27.713$ GHz, $B_w = 8$ GHz (equi-ripple frequency bandwidth), and the orange line corresponds to $f_c = 27.928$ GHz, $B_w = 4$ GHz (equi-ripple frequency bandwidth). $n = 4$ and $S_{11} < -20$ dB for both cases. As shown in the calculation results, the loss is due to the wide bandwidth. In this case, $Q_e = 6.5$ for the 4 GHz band, while $Q_e = 3.2$ for the 8 GHz band. TheQ_e is small for wide band BPF, typically resulting in low-loss transmission characteristics. Thus, this method can be used to investigate Q_e of various metasurface structures to determine the viability of broadening the unit cell bandwidth for lower loss.

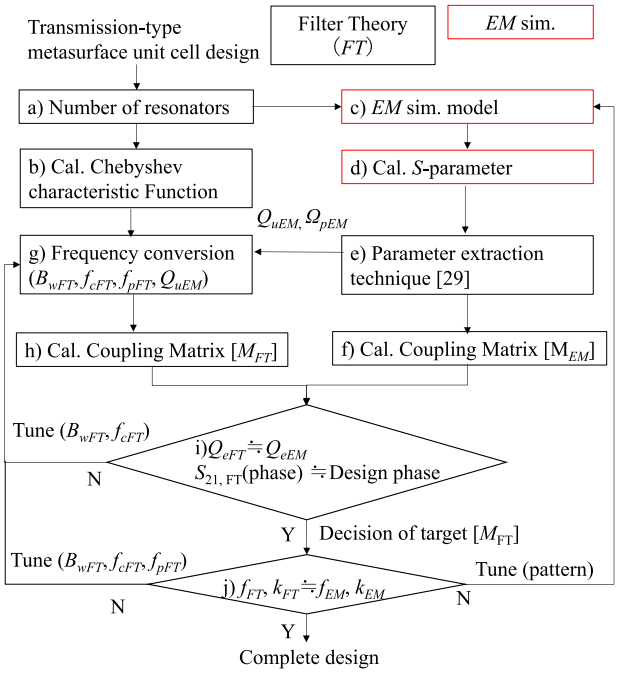

Fig. 7 Design flow

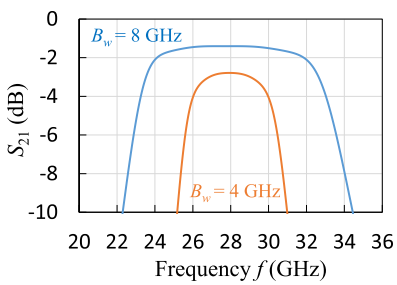

Fig. 8 Loss of cell versus bandwidth for $B_w = 4$ GHz and $B_w = 8$ GHz with $Q = 58$.

3. Design Results of Refractive Plates

3.1 Unit Cell Design by Design Flow

Here, the design flow is demonstrated with unit cell U(180) as an example. First, steps a) to j) are applied to the structure shown in Fig. 4, and the results are shown in Fig. 9. The S-parameters are calculated by fitting the transfer function using the parameter extraction method [29]. In addition, $Q_{uEM} = 58$ and $\Omega_{pEM} = 1.57, 1.12$ are also calculated using $n = 4$, $f_{cEM} = 24.525$ GHz, and $B_{wEM} = 13.38$ GHz (half-power frequency bandwidth). As shown in the lower right of Fig. 9, the coupling matrix is computed from the above parameters. Despite the symmetric structure, the resonant frequencies at the symmetric positions, such as $f_{11} = 21.755$ GHz and $f_{44} = 21.749$ GHz, are different in the extracted coupling matrix due to the errors in the fitting program. In particular, the values of Q_u of the four resonators are the same in this calculation for approximation,

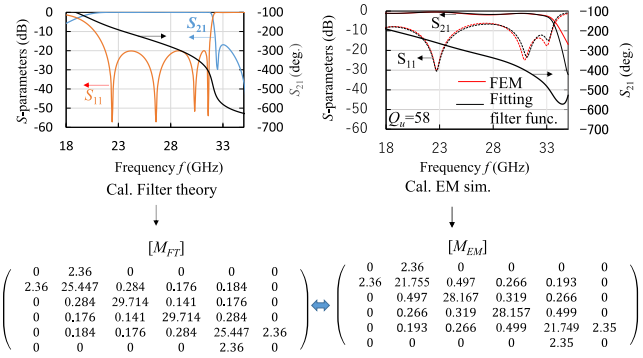

Fig. 9 Theoretical calculation and simulation results for the initial structure of the unit cell without adjusting the coupling structure. The diagonal elements in coupling matrices are in GHz.

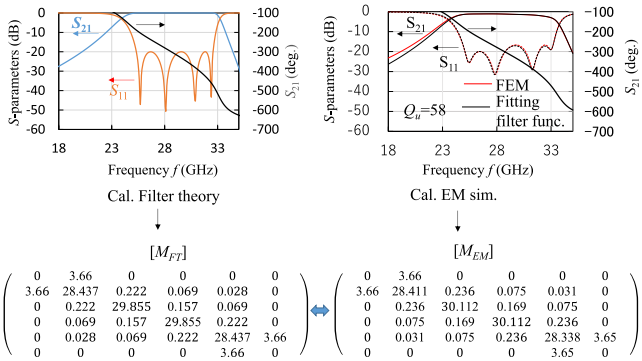

Fig. 10 Theoretical calculations and simulation results for the final structure of the unit cell. The diagonal elements in coupling matrices are in GHz.

although they should be different from each other.

The filter theory calculations are adjusted by B_{wFT} so that Q_{eFT} is similar to Q_{eEM} of the coupling matrix. $S_{21,FT}$(phase) is adjusted by B_{wFT} and f_{cFT} so that $U(180) = -280°$. Figure 9 shows the resulting S-parameters and coupling matrix calculated under the following conditions: $n = 4$, $f_{cFT} = 24.525$ GHz, $B_{wFT} = 13.38$ GHz (half-power frequency bandwidth), $S_{11} < -20$ dB, and lossless.

Both the resonant frequencies and coupling coefficients of the above matrices were found to be different. This implies that good reflection characteristics throughout the passband can be obtained by controlling the coupling coefficient.

Steps a)-j) are applied to the structure in Fig. 5, which contains patterns to adjust the frequencies f_{cEM} and the coupling coefficients k_{EM}. Here, steps c) to j) are repeated multiple times. Figure 10 shows the calculation results for the final design of the unit cell U(180). Finally, the values of $f_{cEM} = 28.005$ GHz, $B_{wEM} = 9.81$ GHz (half-power frequency bandwidth), $Q_u = 58$, and $\Omega_{pEM} = 1.86$, 3.08 are extracted. The following conditions are considered for calculating S-parameters and $[M_{FT}]$: $n = 4$, $f_{cFT} = 28.082$ GHz, $B_{wFT} = 9.64$ GHz (half-power frequency bandwidth), $S_{11} < -20$ dB and lossless. The resonant frequencies and coupling coefficients obtained from *EM* simulation are close to similar to the corresponding theoretical calculations. $S_{21,EM}$(phase) is adjusted to be $-270°$.

3.2 Loss Calculations for the Proposed Structure

The conductivity in the millimeter wave band is lower than that in the microwave band due to the rough interface between the dielectric and conductor [31], [32]. This effect is confirmed by *EM* simulation for the unit cell $U(180)$ shown in the previous section. The extracted values of f_{cEM}, B_{wEM} (half-power frequency bandwidth), and Ω_{pEM} are the same as those used in Fig. 10. The Q value due to conductor loss, Q_c, is calculated using the parameter extraction method [29] to determine the results of *EM* simulation with varying conductivity. The Q_c values do not include reflection losses as they are obtained by fitting the transmission and reflection

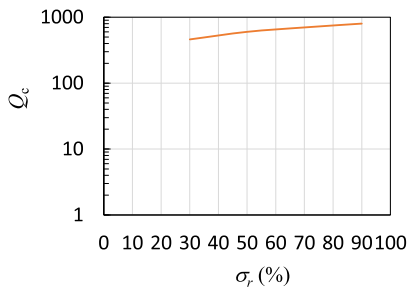

Fig. 11 Q_c due to conductor losses in the unit cell.

characteristics. Figure 11 shows the calculated Q_c values. No extreme decrease in Q_c value was observed with the decrease in conductivity.

The same also confirms the effect of Q due to dielectric loss, Q_d. $Q_c = 600$ at $\sigma = 2.9 \times 10^7$ S/m ($\sigma_r = 50\%$) was used as a typical conductor loss in the prototype design. The unloaded quality value of Q_u for the total loss of the unit cell is given by

$$\frac{1}{Q_u} = \frac{1}{Q_c} + \frac{1}{Q_d} \tag{5}$$

As shown in Fig. 12, the loss of the unit cell, $\tan\delta$, is calculated by substituting the Q_u factor into Eq. (4). In this prototype, FR4 is selected for lower cost. Nevertheless, its loss of $\tan\delta = 0.015$ is directly related to the loss of the unit cell. The Q_u factor for a typical low-loss material with $\tan\delta = 10^{-3}$ in the millimeter wave band is improved to $Q_u = 375$, as shown in Fig. 12. Theoretical calculations using Eq. (4) give an insertion loss of 0.17 dB.

EM simulation of the unit cell $U(180)$ is conducted using $\sigma_r = 50\%$ and $\tan\delta = 10^{-3}$, and the results are shown in Fig. 13. However, the simulation does not consider the difference in unloaded Q factors of the four resonators. The *EM*-simulated insertion loss shows 0.2 dB at 28 GHz, and this finding is in agreement with the theoretical calculations. This demonstrates that the loss of the unit cell can be obtained by treating the loss as a Q_u factor and performing filter theory calculations.

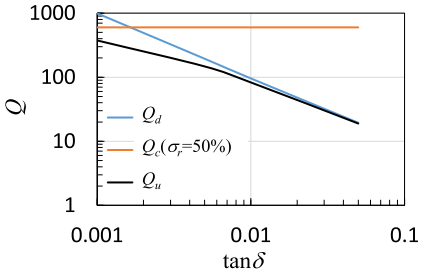

Fig. 12 Q due to total loss of the unit cell.

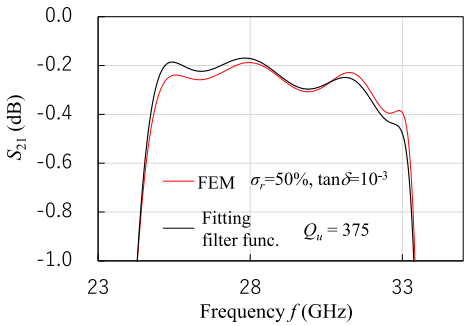

Fig. 13 Unit cell loss at $\sigma_r = 50\%$ and $\tan\delta = 10^{-3}$ by EM simulation.

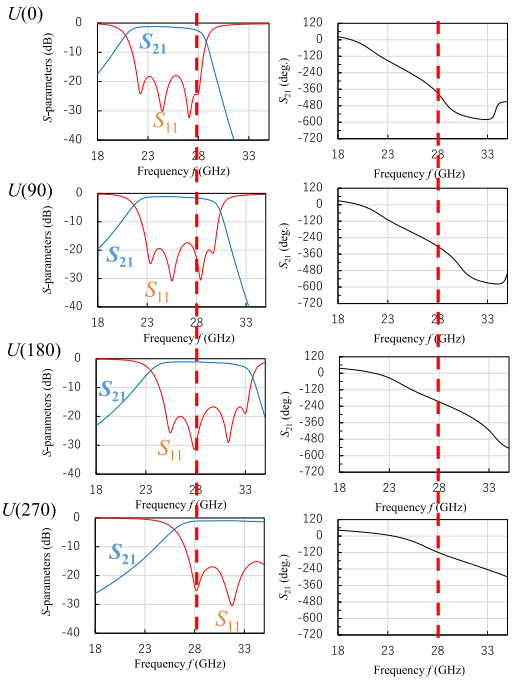

Fig. 14 Calculated results of cells in the refractive plate.

Table 1 Layer pattern size of unit cells (in mm)

layer	1 and 7	2 and 6	3 and 5	4
	W_1	W_2	W_1	W_2
0°	2.020	1.500	2.000	1.848
90°	1.895	1.500	1.860	1.748
180°	1.695	1.500	1.645	1.748
270°	1.410	1.500	1.360	1.748

3.3 Four Unit Cell Design Results

Based on the unit cell shown in Fig. 5, four different unit cells were designed to form supercells. The widths of the odd-layer square electrode patch (W_1) and the even-layer square dielectric aperture (W_2), in mm, are given in Table 1. The widths of the cross-shaped sections (W_3) of the even layers are all 0.1 mm.

Figure 14 shows the characteristics of each unit cell in the supercell, calculated by using the *EM* simulator based on FEM. The graphs in the middle of the figure represent the transmission and reflection characteristics. The graphs on the right side of the figure represent the phase characteristics of transmission coefficients. The dashed line is placed at 28 GHz, indicating that frequency conversion was used in the design. Here, each cell is designed using the periodic boundary conditions of FEM, and the desired refraction is achieved by tuning BPF center frequencies. The calculated phases of the four cells are $U(0) = -388°$ (reference), $U(90) = -307°$ (89°), $U(180) = -208°$ (180°), and $U(270) = -118°$ (270°). The reference phase planes in the EM simulation shift to 13.5 mm from the Floquet port position. Here, the differences between the absolute values of the phases obtained by theoretical calculation and those by *EM* simulation are corrected in the extracted calculation of theoretical results.

Consequently, a 4th-order wide band BPF characteristic and a low-loss passband characteristic are achieved even with the commonly used FR4 substrate. Further loss improvement in the passband characteristics can be achieved by broadening the bandwidth and using low-loss materials.

3.4 Refractive Plate Design Results

The simulation model of the refractive metasurface plate constructed using four cells is calculated. The realized gain (RG) of the two models is calculated to evaluate the loss of the refractive metasurface plate. FR4 substrate is used for RG_{loss}, while $\tan\delta = 0$ and $\sigma = \infty$ for $RG_{lossless}$. Figure 15 shows the ratio of $RG_{loss}/RG_{lossless}$. Here, the yz plane is the cut plane of the radiation patterns. As shown in Fig. 15 (a) (b), the refractive angle is in the desired direction of 45°. Compared to the lossless material condition, the loss is 1.8 dB for x-polarization at the Floquet Port and 1.9 dB for y-polarization at the Floquet Port for the FR4 substrate. For both x-polarization and y-polarization, S_{11} at 28 GHz is above −20 dB, and the effect of reflection loss is negligible. The side lobes at 0° and −45° and the energy scattered into the direction of Floquet harmonics at the design frequency are described in details in a previous study [13].

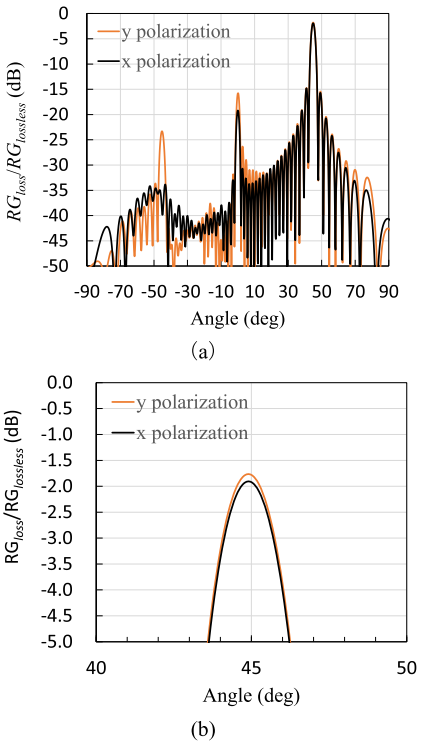

Fig. 15 Calculation results for the ratio of realized gain (RG_{loss}/$RG_{lossless}$) of 79 cells. (a) Calculation results for the x and y polarization RG ratio. (b) Enlarged view.

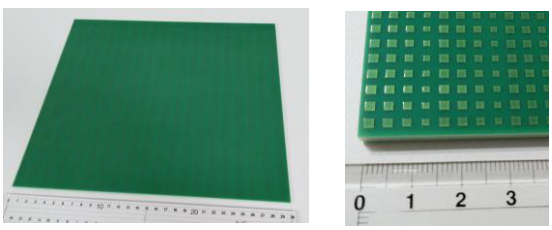

Fig. 16 Photograph of the refractive plate prototype.

4. Measurement Results of Refractive Plates

Figure 16 shows a prototype of the refractive metasurface plate, measuring 300 mm × 275 mm × 3.006 mm. The structure consists of periodically aligned supercells. Figure 17 shows the experimental environment. An anechoic chamber is used to conduct the measurements. A radio wave absorber was placed on both sides of the metasurface plate in the chamber to suppress direct wave effects between the transmitting and receiving antennas (horn antennas with 15 dBi). Due to the limitations of the measurement system, the distance between the transmitting antenna and the plate 3050 mm, while the distance between the plate and the receiving antenna was 750 mm.

Here, the input power was not clear since the refractive plate was apart from the transmitting antenna. Thus, the refractive plate was placed between the transmitting and receiving antennas, and S_{21} was measured instead. In addition, S_{21} without the plate was measured as a reference [13]. Far field conditions are considered as the measurement required plane waves. However, this measurement did not provide sufficient distance. The conditional expression for R, i.e., the approximate distance that can be regarded as the far field, is shown below [33]:

$$R > 2\frac{D^2}{\lambda} \tag{6}$$

where D denotes the largest dimension of either antenna. When the diagonal length of the refractive plate (0.41 m)

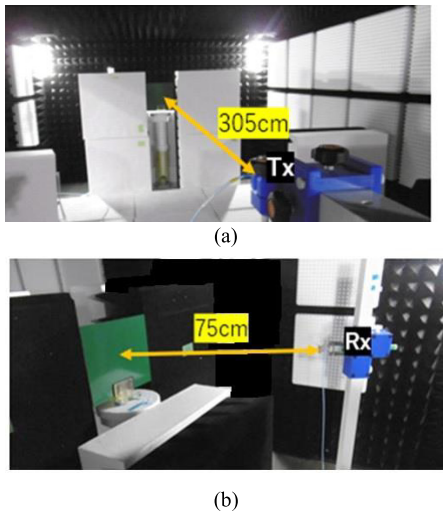

Fig. 17 Experimental environment. (a) Transmitting antenna Tx to refractive plate. (b) Refractive plate to receiving antenna Rx.

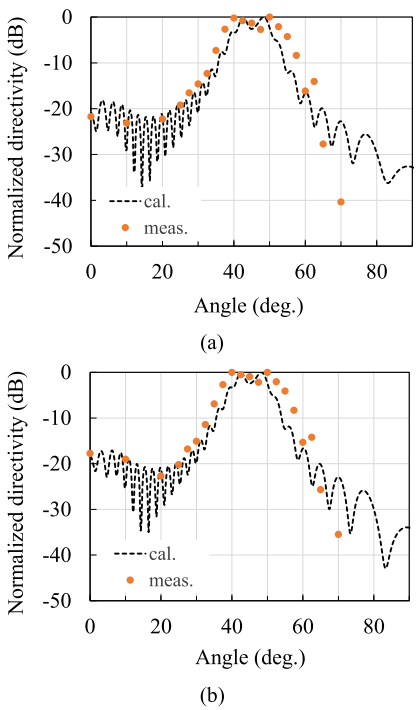

Fig. 18 Measurement and calculation results for refractive plates for (a) x and (b) y polarizations.

is used as D, $R > 31$ m. In comparison, the distance between the refractive plate and the receiving antenna was quite close. Therefore, the results proved to be invalid as the peak was split with respect to the reference measurement of the far field.

The directivity obtained from Poynting vectors of the near field by FEM at 750 mm between the plate and the receiving antenna denotes the recalculated results for the model. Figure 18 presents a comparison between the simulated and measured results for the normalized directivity of x and y polarization of this plate. The measured directivity was normalized to the maximum S_{21} value of directivity. Our findings showed that the calculated and measured results are in good agreement, with directional peaks in the desired 45° direction. The close distance between the plate and the receiving antenna, which is the Fresnel region, results in the split peak in the 45° direction. The prototype plate operates in both types of polarization because the x and y polarization show the same characteristics in Fig. 18. These results confirm that the refractive plate operated as intended and validated the design theory.

5. Conclusion

In this study, we applied the filter theory to design the transmission-type metasurface cells and proposed a new structure for the metasurface unit cell that adjusts its resonance frequency and coupling coefficient according to the equivalent circuit. We designed and fabricated a refractive transmission-type metasurface plate using the frequency shift of the filter. Our findings showed that the measured and calculated results of the plate are in good agreement, confirming the suitability of applying the filter design method in designing metasurface cells. We believe that the proposed approach will allow us to design more complex metasurface cells in the future. For example, microwave filter design could potentially be applied to the design of dual-band transmission-type metasurface cells.

References

[1] V.G. Ataloglou, M. Chen, M. Kim, and G.V. Eleftheriades, "Microwave Huygens' metasurfaces: fundamentals and applications," IEEE J. Microwaves, vol.1, no.1, pp.374–388, 2021. doi: 10.1109/JMW.2020.3034578.

[2] H. Nakano, S. Mitsui, and J. Yamauchi, "Tilted-beam high gain antenna system composed of a patch antenna and periodically arrayed loops," IEEE Trans. Antennas Propag., vol.62, no.6, pp.2917–2925, 2014. doi: 10.1109/TAP.2014.2311460.

[3] H. Nakano, M. Toida, S. Okabe, and J. Yamauchi, "Tilted beam formation using Parasitic Loop-Based Plates," IEEE Trans. Antennas Propag. Lett., vol.15, pp.1475–1478, 2015. doi: 10.1109/LAWP.2015.2513671.

[4] H. Nakano, Y. Kameta, and J. Yamauchi, "Increased beam tilt angle from a patch antenna with three inhomogeneous loop-based plates," Electronics Lett., vol.53, no.24, pp.1562–1564, 2017. doi: 10.1049/el.2017.3243.

[5] J.-J. Liang, G.-L. Huang, J.-N. Zhao, Z.-J. Gao, and T. Yuan, "Wideband phase-gradient metasurface antenna with focused beams," IEEE Access, vol.7, pp.20767–20772, 2019. doi: 10.1109/ACCESS.2019.2898550.

[6] B.-Q. Lin, J. Guo, Y. Wang, Z. Wang, B. Huang, and X. Liu, "A wide-angle and wide-band circular polarizer using a bi-layer metasurface," PIER, vol.161, pp.125–133, 2018.

[7] D. Kitayama, M. Yaita, and H.-J. Song, "Laminated metamaterial flat lens at millimeterwave frequencies," Opt. Express, vol.23, no.18, pp.23348–23356, 2015. doi: 10.1364/OE.23.023348.

[8] C. Pfeiffer and A. Grbic, "Metamaterial Huygens' surfaces: tailoring wave fronts with reflectionless sheets," Phys. Rev. Lett., PRL, vol.110, no.19, 2013. doi: 10.1103/PhysRevLett.110.197401.

[9] C. Pfeiffer and A. Grbic, "Millimeter-wave transmitarrays for wavefront and polarization control," IEEE Trans. Microw. Theory Techn., vol.61, no.12, pp.4407–4417, 2013. doi: 10.1109/TMTT.2013.2287173.

[10] Y. Wang, Y. Liu, C. Liu, B. Sun, X. Sun, F. Li, and Y. Lu, "New design for transmitted phase of reflectionless metasurfaces with 2π coverage," IEEE Photon. J., vol.7, no.3, pp.1–8, 2015. doi: 10.1109/JPHOT.2015.2440337.

[11] X. Wan, S.L. Jia, T.J. Cui, and Y.J. Zhao, "Independent modulations of the transmission amplitudes and phases by using Huygens metasurfaces," Sci Rep., vol.6, 25639, 2016. doi: 10.1038/srep25639.

[12] M. Chen, E. Abdo-Sánchez, A. Epstein, and G.V. Eleftheriades, "Experimental verification of reflectionless wide-angle refraction via a bianisotropic Huygens' metasurface," Proc. 32nd URSI GASS, Montreal, 2017. doi: 10.23919/URSIGASS.2017.8105103.

[13] A.E. Olk, P.E.M. Macchi, and D.A. Powell, "High-efficiency refracting millimeter-wave Metasurfaces," IEEE Trans. Antennas Propag., vol.68, no.7, pp.5453–5462, 2020. doi: 10.1109/TAP.2020.2975840.

[14] J. Yang, X. Wu, J. Song, C. Huang, Y. Huang, and X. Luo, "Cascaded metasurface for simultaneous control of transmission and reflection," Opt. Express, vol.27, no.6, pp.9061–9070, 2019. doi: 10.1364/OE.27.009061.

[15] Q. Ma, L. Chen, H.B. Jing, Q.R. Hong, H.Y. Cui, Y. Liu, L. Li, and T.J. Cui, "Controllable and programmable nonreciprocity based on detachable digital coding metasurface," Adv. Opt. Materials, vol.7, no.24, p.1901285, 2019. doi: 10.1002/adom.201901285.

[16] R.Y. Wu, L. Bao, L.W. Wu, and T. Cui, "Broadband transmission–type 1-bit coding metasurface for electromagnetic beam forming and scanning." Sci. China-Phys. Mech. Astron., vol.63, no.8, 2020. doi: 10.1007/s11433-019-1479-3.

[17] M. Selvanayagam and G.V. Eleftheriades, "Circuit modeling of Huygens surfaces," IEEE Trans. Antennas Propag. Lett., vol.12, pp.1642–1645, 2013. doi: 10.1109/LAWP.2013.2293631.

[18] A. Epstein and G.V. Eleftheriades, "Passive lossless Huygens metasurfaces for conversion of arbitrary source field to directive radiation," IEEE Trans. Antennas Propag., vol.62, no.11, pp.5680–5695, 2014. doi: 10.1109/TAP.2014.2354419.

[19] M. Chen, E. Abdo-Sánchez, A. Epstein, and G.V. Eleftheriades, "Theory, design, and experimental verification of a reflectionless bianisotropic Huygens' metasurface for wide-angle refraction," Phys. Rev. B, vol.97, no.12, 125433, 2018. doi: 10.1103/PhysRevB.97.125433.

[20] S.S. Bukhari, W.G. Whittow, J.C. Vardaxoglou, and S. Maci, "Equivalent circuit model for coupled complementary metasurfaces," IEEE Trans. Antennas Propag., vol.66, no.10, pp.5308–5317, 2018. doi: 10.1109/TAP.2018.2860052.

[21] W. Ji, T. Cai, Z. Xi, and P. Urbach, "Highly efficient and broadband achromatic transmission metasurface to refract and focus in microwave region," J. Laser Photonics Rev., vol.16, no.1, 2021. doi: 10.1002/lpor.202100333.

[22] T. Brown, Z. Liu, and P. Mojabi, "Full-wave verification of an electromagnetic inversion metasurface design method," Proc. IEEE Int. Symp. Antennas Propag. Radio Sci. Meet., pp.971–972, 2020. doi: 10.1109/IEEECONF35879.2020.9330280.

[23] A.E. Williams, "A four-cavity elliptic waveguide filter," IEEE Trans. Microw. Theory Techn., vol.18, no.12, pp.1109–1114, 1970. doi: 10.1109/TMTT.1970.1127419.

[24] R.J. Cameron, "Advanced coupling matrix synthesis techniques for microwave filters," IEEE Trans. Microw. Theory Techn., vol.51, no.1, pp.1–10, 2003. doi: 10.1109/TMTT.2002.806937.
[25] S. Tamiazzo and G. Macchiarella, "An analytical technique for the synthesis of cascaded N-tuplets cross-coupled resonators microwave filters using matrix rotations," IEEE Trans. Microw. Theory Techn., vol.53, no.5, pp.1693–1698, 2005. doi: 10.1109/TMTT.2005.847065.
[26] M. Ohira and Z. Ma, "An efficient design method of microstrip filtering antenna suitable for circuit synthesis theory of microwave bandpass filters," Proc. IEEE Int. Symp. Antennas Propag., 15919173, 2015.
[27] P. Harscher and R. Vahldieck, "Automated computer-controlled tuning of waveguide filters using adaptive network models," IEEE Trans. Microw. Theory Techn., vol.49, no.11, pp.2125–2130, 2001. doi: 10.1109/22.963147.
[28] P. Harscher, R. Vahldieck, and S. Amari, "Automated filter tuning using generalized low-pass prototype networks and gradient- based parameter extraction," IEEE Trans. Microw. Theory Techn., vol.49, no.12, pp.2532–2538, 2001. doi: 10.1109/22.971646.
[29] A. Garcia-Lamperez, S. Llorente-Romano, M. Salazar-Palma, and T.K. Sarkar, "Efficient electromagnetic optimization of microwave filters and multiplexers using rational models," IEEE Trans. Microw. Theory Techn., vol.52, no.2, pp.508–521, 2004. doi: 10.1109/TMTT.2003.822021.
[30] J. Li, T. Wu, W. Xu, Y. Liu, C. Liu, Y. Wang, Z. Yu, D. Zhu, L. Yu, and H. Ye, "Mechanisms of 2π phase control in dielectric metasurface and transmission enhancement effect." Opt. Express, vol.27, no.16, p.23186–23196, 2019. doi: 10.1364/OE.27.023186.
[31] N. Hirayama, A. Nakayama, H. Yoshikawa, T. Shimizu, and Y. Kogami, "Measurement technique for interface and surface conductivities at millimeter-wave frequencies using dielectric rod resonator excited by nonradiative dielectric waveguide," IEEE Trans. Microw. Theory Techn., vol.70, no.5, pp.2750–2761, 2022. doi: 10.1109/TMTT.2022.3157301.
[32] G. Gold and K. Helmreich, "A physical surface roughness model and its applications," IEEE Trans. Microw. Theory Techn., vol.65, no.10, pp.3720–3732, Oct. 2017. doi: 10.1109/TMTT.2017.2695192.
[33] C.A. Balanis, "Antenna theory analysis and design," Published by John Wiley & Sons, Inc., Canada, 4-47, p.161, 2016.

Hiromichi Yoshikawa received the B.E., M.E., and Ph.D. degrees from Saitama University, Saitama, Japan, in 1996, 1998, and 2001, respectively. In 2001, he joined Kyocera Corporation, Japan, where he has been engaged in research and development of measurement methods and designs of antenna and filters at microwave and millimeter-wave frequencies. Dr. Yoshikawa is a member of the Institute of Electronics Information and Communication Engineers (IEICE), Japan.

Nobuki Hiramatsu received the B.S. and M.S. degrees in earth science from Kyoto University, Kyoto, Japan, in 1991 and 1993, respectively. He received the M.S. degree in electrical engineering from the University of Arizona, Tucson, in 2011. In 1993, he joined Kyocera Corporation, Kyoto, Japan. He was involved in millimeter wave circuit design using low-loss ceramic waveguides and multilayered ceramic substrates, and later in research on small antennas. His current research interests include metasurface technologies for microwave and millimeter-wave frequencies.

Masamichi Yonehara received the B.E. and M.E. degrees in electronic device engineering from Yamaguchi University, Yamaguchi, Japan, in 2015 and 2017, respectively. In 2017, he joined Kyocera Corporation, Kyoto, Japan. He was involved in microwave and millimeter-wave antenna design using metamaterial technologies. His current research interests include metasurface technologies for microwave and millimeter-wave frequencies. He is a member of the Insutitute of Electronics Information and Communication Engineers (IEICE), Japan.

Hisamatsu Nakano has been with Hosei University since 1973, where he is currently a Professor Emeritus and a Special-appointment Researcher with the Electromagnetic Wave Engineering Research Institute attached to the graduate school. He has held positions as Visiting Associate Professor at Syracuse University (March to September 1981), and Visiting Professor at the University of Manitoba (March to September 1986), University of California, Los Angeles (September 1986 to March 1987), and Swansea University, U.K. (July to September of 2016 to 2019). He has published over 360 articles in peer- reviewed journals and 11 books/book chapters, including Low-profile Natural and Metamaterial Antennas (IEEE Press, Wiley, 2016). His significant contributions are the development of five integral equations for line antennas in free space and printed on a dielectric substrate, the invention of an L-shaped wire/strip antenna feeding method, and the realization of numerous wideband antennas, including curl, metaspiral, metahelical, and Body of Revolution antennas. His other accomplishments include design of antennas for GPS, personal handy phones, space radio, electronic toll collection, RFID, UWB, and radar. He has been awarded 78 patents, including A Curl Antenna Element and Its Array (Japan). His research topics include numerical methods for low- and high-frequency antennas and optical waveguides. He served as a member of the IEEE APS Administrative Committee from 2000 to 2002 and a Region 10 Representative from 2001 to 2010. He received the H.A. Wheeler Award in 1994, the Chen-To Tai Distinguished Educator Award in 2006, and the Distinguished Achievement Award in 2016, all from the IEEE Antennas and Propagation Society. He was also a recipient of The Prize for Science and Technology from Japan's Minister of Education, Culture, Sports, Science and Technology in 2010. Most recently, he was selected as a recipient of the Antenna Award of the European Association on Antennas and Propagation (EurAAP) in 2020. He is an Associate Editor of several scientific journals and magazines, including Electromagnetics.